Electrochemical noise analysis of cavitation erosion corrosion resistance of NbC nanocrystalline coating in a 3.5 wt% NaCl solution

Shuang Peng [a], Jiang Xu [a,*], Zhengyang Li [b], Shuyun Jiang [c], Zong-Han Xie [d], Paul Munroe [e]

[a] Department of Material Science and Engineering, Nanjing University of Aeronautics and Astronautics, 29 Yudao Street, Nanjing 210016, PR China
[b] Institute of Mechanics, Chinese Academy of Sciences, Beijing 100190, PR china
[c] Department of Mechanical Engineering, Southeast University, 2 Si Pai Lou, Nanjing 210096, PR China
[d] School of Mechanical Engineering, University of Adelaide, SA 5005, Australia
[e] School of Materials Science and Engineering, University of New South Wales, NSW 2052, Australia

A B S T R A C T

To combat cavitation erosion-corrosion damage inflicted upon mechanical components in marine applications, NbC nanocrystalline coatings were synthesized by a double cathode glow discharge assisted reactive sputtering method. The coating comprised equiaxed B1-NaCl-type NbC grains with an average grain size of ~10 nm and a strong NbC (200)-oriented texture by TEM observation. The electrochemical response of the coating exposed to a 3.5 wt% NaCl solution with and without the influence of cavitation was monitored by electrochemical noise (EN) measurements, in addition to open circuit potential and cyclic polarization. To differentiate the cavitation erosion-corrosion resistance between the NbC coating and a reference Ti-6Al-4V alloy substrate, the EN data were further evaluated, based on a series of analyses, including frequency domain, time-domain, shot noise and wavelet transform. For the Ti-6Al-4V alloy, with increasing output power, the noise resistance (R_n) and slope (k values) of potential and current power spectral density (PSD) decreased, and the average charge in each corrosion event (q) and the total energy of d series crystals increased markedly at the output power levels above 400 W, indicative of a high propensity of pitting corrosion for this alloy. Conversely, the R_n and k values for the NbC coating were found to be almost independent of the output power, and the charge of the corrosion event and the total energy of the d series crystals were much lower than that of the Ti-6Al-4V alloy. The findings garnered from analyzing the EN signals is in accord with what were uncovered from examining the eroded surface morphologies, suggesting that the EN method might offer a reliable and effective tool to probe the cavitation erosion-corrosion behavior in developing durable material.

1. Introduction

Cavitation is a long-standing problem that occurs on flow-handling components operating in hydrodynamic environment, where the formation and implosion of vapor bubbles take place as a result of frequent pressure fluctuations in high velocity fluid or vibrating liquids [1]. Cavitation damage in non-corrosive media is, essentially, mechanical disruption induced by impingement of high-speed micro-jets and shock waves resulting from the collapse of vapor bubbles [2]. However, when these components operate in aggressive flowing fluids (e.g., in marine environments), the cavitation deterioration process is often complicated by the combined action of electrochemical corrosion and mechanical erosion, often termed cavitation erosion-corrosion. Under such

condition, these two deleterious factors mutually reinforce and cause far more damage than the sum of these effects operating separately [3,4]. For example, for some passivating metals, such as titanium alloys and stainless steels, mechanical erosion exacerbates the rate of removal of the protective passive film and thus, the underlying fresh surface is exposed to corrosive attack, so accelerating the cavitation corrosion process [5,6]. Since cavitation erosion-corrosion is a form of surface destruction that strongly correlates with surface chemical, physical and mechanical properties of a material, a cost-effective and feasible strategy to combat such a phenomenon is to fabricate appropriate protective surface coatings and hence extend service lifetime of components [7]. Among a variety of surface modification technologies at present, the double cathode glow discharge deposition technique has been proven to

* Corresponding author.
  E-mail address: xujiang73@nuaa.edu.cn (J. Xu).

be an effective approach to improve the mechanical and electrochemical properties of the substrate material through the deposition of nanocrystalline metal silicide and ceramic coatings [8,9]. In our previous work, both of the TaSi$_2$ and NbN nanocrystalline coatings has been validated to have a favorable improvement for the cavitation-erosion resistance [10,11].

Owing to their unique chemical and physical properties, carbides of transition metals have found a wide range of industrial applications, such as hard coatings in cutting tools, diffusion barriers in electronics, metallic interconnects, field emitters and structural components in aerospace vehicles [12]. Among them, NbC has drawn more attention over the past few years due to its outstanding properties, including excellent electrical conductivity, high hardness and good corrosion resistance [13]. Most notably, NbC is considered as an ideal candidate as a coating material for structural applications, where resistance to attack by corrosion and wear is a requirement [14]. However, to the authors' knowledge, there are no prior reports in the literature describing the cavitation behavior of NbC in hostile conditions, either as a bulk material or in coating form.

Commonly, many published studies on cavitation erosion-corrosion present a qualitative analysis of the morphology of the cavitation surface together with a quantitative measurement of cumulative weight loss [15,16]. In general, the cavitation erosion-corrosion process can be divided into three different regimes: an incubation stage, an accumulation stage and a steady-state stage [17]. A clear limitation of the aforementioned approaches is that, during the incubation stage, the weight loss and any changes in surface morphologies are less apparent, since only elastic deformation or small amounts of plastic deformation take place on the surface. To obtain a deeper understanding of the mechanisms responsible for the cavitation erosion-corrosion process, various electrochemical tests, such as electrochemical impedance spectroscopy (EIS) and direct current (DC) resistance measurements, have been used to correlate the electrochemical response of a material with its cavitation erosion-corrosion resistance [18,19]. Because the cavitation erosion-corrosion is a form of instantaneous and localized attack, it is necessary to employ continuous corrosion monitoring of cavitation damage. Unfortunately, the above-mentioned electrochemical techniques are not suitable for this approach. For instance, EIS measurements are carried out under stationary liquid conditions and thus it is not feasible to monitor the cavitation process in real time [18].

Electrochemical noise (EN), defined as the spontaneous fluctuations in potential or current that occur at the interface between the electrode and electrolyte, has been widely adopted to probe mechanistic insights of a corroding system through real-time analysis of different localized corrosion processes, including breakdown and self-healing of passive films, metastable and propagating pitting, crevice corrosion, stress corrosion cracking, etc. [20]. Compared with other electrochemical methods, EN does not require any artificial potential perturbation and thus provides a simple way to perform on-line monitoring [21]. Wood et al. [22] investigated the erosion–corrosion properties of stainless steels and thermal spraying coatings using electrochemical noise measurements. The results showed that the EN signals could directly signify the evolving corrosion steps under erosion–corrosion conditions, such as electrolyte permeation of the coating or coating breakdown. Therefore, the EN technique appears to be a promising avenue to uncover the responses of a material to cavitation damage.

In this study, a NbC nanocrystalline coatings were deposited on a Ti-6Al-4V substrate (a reference alloy for marine application) in an effort to enhance its cavitation erosion-corrosion resistance. Following the microstructural and mechanical characterization, the cavitation erosion-corrosion experiments were performed on the NbC nanocrystalline coating and uncoated Ti-6Al-4V, with both exposed to a 3.5 wt% NaCl solution (simulating marine environment) by various electrochemical techniques, with emphasis on elucidating the critical role of capturing and mining EN signals to decipher complex cavitation-corrosion processes.

2. Experimental procedure

2.1. Coatings preparation

A commercially available Ti-6Al-4V disk, with dimensions $\Phi20 \times 3$ mm, was used as the substrate material. The substrates were mechanically ground on a series of SiC abrasive papers (from 250 # to 1200 #) to remove surface oxides and then polished with 0.5 μm Cr$_2$O$_3$ powder, followed by cleaning in an ultrasonic bath using acetone as a solvent. A double-cathode glow discharge apparatus was employed to prepare the NbC nanocrystalline coating in a vacuum chamber with a base pressure of 5×10^{-4} Pa. A sputtering target with dimensions of $\Phi70 \times 5$ mm was fabricated from a ball-milled equimolar mixture of Nb (300 mesh, >99.9% purity) and graphite powders (300 mesh, >99.9% purity) via cold compaction under an applied pressure of 600 MPa. During the deposition process, high-purity Ar gas served as a working gas and filled the chamber to maintain a working pressure of 35 Pa. The target bias voltage and substrate bias voltage were set to −900 V and -300 V, respectively. The parallel distance between the target and the substrate sample was kept at 8.5 mm and the deposition temperature was held at 650 °C with deposition time of 3 h.

2.2. Microstructure characterization

The crystal structure of the as-received coating was determined by means of an X-ray diffractometer (XRD, Bruker, D8 Advance) using Cu-Kα radiation (λ = 0.154 nm) operated at 30 mA and 40 kV. The measurements were carried out at a scan rate of 10°/min over a range of 2θ angle values from 20° to 90°. Both the cross-sectional microstructure and eroded surface morphologies of the coatings were examined via a field-emission scanning electron microscope (FE-SEM Hitachi, S-4800, Japan) which incorporated an energy dispersive spectrometer (EDS) (EDX-4, Philips). A JEOL JEM-2010 transmission electron microscope (TEM), operating at an accelerating voltage of 200 kV, was used to characterize plan-view TEM samples obtained from the coating that were fabricated by grinding, dimpling and, as a final single-jet, electrochemical polishing from the uncoated side of the sample. X-ray photoelectron spectroscopy (XPS) analysis was performed using an ESCALAB 250 spectrometer analyzer (Thermo VG Co, USA) with an Al Kα X-ray source (hν = 1486.68 eV). Peak positions were calibrated with reference to the adventitious C1s peak that is located at a binding energy of 284.6 eV and peak identification was accomplished by reference to an XPS database.

2.3. Nanoindentation and scratch test

Nanoindentation testing and scratch adhesion testing were performed on the surface of the as-deposited coating to investigate the mechanical properties of the coating. The nanoindentation test was conducted at a loading rate of 40 mN/min and to a maximum load of 40 mN using a nanoindentation tester (Ultra-Micro Indentation System 2000). A pyramidal Berkovich diamond indenter was employed. The hardness, H, and elastic modulus, E, of tested samples were determined from the indentation data using the Oliver and Pharr method [23]. Five indentations were conducted on each specimen to ensure reliability of the experimentally acquired data. The adhesion strength of the coating to the Ti-6Al-4V substrate was determined using a scratch tester (WS-2005) that employed an acoustic emission (AE) detector. During the scratch test, the as-deposited coating was scratched with a diamond Rockwell C diamond indenter (radius of 200 μm) at a speed of 5 mm/min. The applied normal load linearly increased from 0 to 100 N at a constant loading rate of 20 N/min. The cohesion strength between the coating and substrate is defined as the critical load (Lc), which is determined by both the intensity of the acoustic signal and the surface morphologies of the scratch tracks observed by SEM analysis.
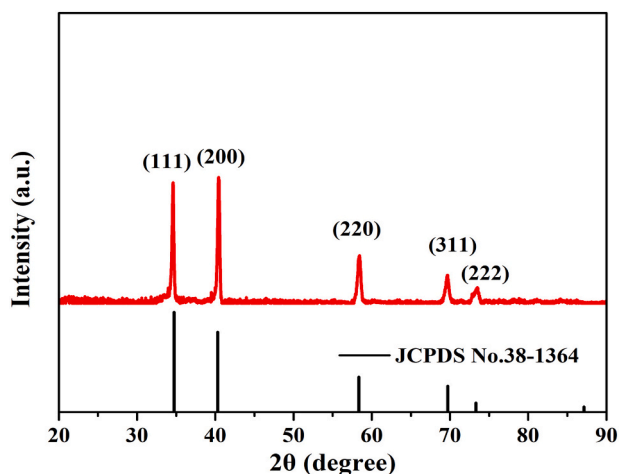
Fig. 1. Typical XRD patterns recorded from NbC-coated Ti-6Al-4V.

Table 1

The calculated crystallite size and the texture coefficients (TC$_{hkl}$) based on each crystallographic plane of the NbC phase.

	(111)	(200)	(220)	(311)	(222)
D (nm)	24.5	22.2	14.8	15.0	9.4
TC$_{hkl}$	0.94	1.21	0.93	0.82	0.74

reported results are the mean values of the parallel experimental data.

3. Results and discussion

3.1. Phase composition and microstructure of NbC coating

Fig. 1 presents a typical XRD spectrum recorded from the NbC coated Ti-6Al-4V alloy. The XRD diffractogram shows only one set of characteristic diffraction peaks over a 2θ angle range from 20° to 90°. The peaks are in good agreement with the JCPDS's data (No. 38-1364) for NaCl-structure cubic δ-NbC phase. Evidently, the (111) and (200) peaks for δ-NbC are the most intense and the ratio of the peak intensity of the (111) reflection to the (200) reflection is slightly different from that expected in the standard powder diffraction pattern, suggesting that the coating may exhibit a preferred crystallographic texture. The degree of texture for the coating can be estimated by the texture coefficient (TC$_{hkl}$) for a given (hkl) plane, which is expressed as [24]:

2.4. Cavitation erosion-corrosion test

Cavitation tests in 3.5 wt% NaCl solution were conducted according to the ASTM G32–10 standard method using a JY92-IIDN magneto-strictive-induced cavitation apparatus (NingBo Scientz Biotechnology Co., Ltd.), as described elsewhere [10]. During cavitation tests, different cavitation intensities were available by controlling the output power of the ultrasonic generator, and the output frequency and peak-to-peak amplitude were fixed at 20 kHz and 60 μm, respectively. The specimen was submerged in the test electrolyte to a depth of 20 mm with the distance between a vibrating horn and test specimen being 0.5 mm. The temperature of the test electrolyte was kept at 25 ± 1 °C controlled by flowing cooling water.

2.5. Electrochemical measurements

All electrochemical experiments were performed on a CHI660E workstation (Shanghai ChenHua Instruments Inc., China). A standard three-electrode cell configuration was used for open circuit potential and potentiodynamic cyclic polarization measurements, where a platinum foil, a saturated calomel electrode (SCE) and the specimen, with an exposed area of 1.0 cm^2, were used as auxiliary electrode, reference electrode and working electrode, respectively. In this work, all electrode potentials were referenced to the SCE. The open circuit potential of the specimen was measured under cavitation cycle conditions (that is, alternating periods of cavitation for 90 s and then quiescence for 30 s). The potentiodynamic cyclic polarization measurements were carried out under continuous cavitation mode. The potential was scanned from a potential 300 mV lower than the value of E$_{corr}$ to 1.7 V with a scan rate of 1 mVs^{-1}.

During the EN experiments, a pair of nominally identical samples was employed as the working electrodes with each exposed area of 0.3 × 1 cm^2. To ensure the same cavitation condition for the pair of samples, both of them were placed parallel below the tip of the vibrating horn with the same distance of 0.5 mm. A SCE was used as the reference electrode. The potential noise from one working electrode was recorded with respect to the SCE and, simultaneously, the current noise was obtained from the galvanic coupling current between the two working electrodes measured by a zero-resistance ammeter system. After 6 h of either static immersion or cavitation erosion-corrosion in a 3.5 wt% NaCl solution, the EN signals were collected from the tested samples over a period of 1024 s with a time interval of 0.1 s. A five-order polynomial fitting method was used to remove the direct current (dc) drift from the original electrochemical noise data. To ensure an acceptable reproducibility of the results, all electrochemical measurements were repeated at least three times at an identical testing condition and the

$$TC_{hkl} = \frac{I_m(hkl)/I_0(hkl)}{\frac{1}{n}\sum_1^n I_m(hkl)\Big/I_0(hkl)} \qquad (1)$$

where TC$_{(hkl)}$ is the texture coefficient, I$_m$(hkl) is peak intensity of (hkl) plane, I$_0$(hkl) is the standard intensity of the same plane obtained from JCPDS data, and n is the number of reflections used. According to Eq. (1), TC$_{(hkl)} > 1$ reflects a preference for a given (hkl) plane. As shown in Table 1, only texture coefficient TC$_{(200)}$ value is larger than 1, confirming that the δ-NbC crystals in this coating prefer to be aligned along the crystallographic a-axis. The texture in a coating depends on the competition between surface and strain energies, ideally acting to minimize the overall free energy [25]. For the B1-NaCl structure coating, the (111) preferred orientation is favored by the strain energy reduction, whereas the (200) preferred orientation is favored by surface energy minimization [26]. Therefore, during the growth of the NbC coating, the surface energy plays a leading role to the total free energy and thus a (200) preferred orientation can be observed. In addition, because the strength along the [200] direction is stronger than along [111] direction [27], it can be expected that a texture growth along (200) direction is good for the NbC coating to achieve higher surface hardness with respect to (111) texture. In addition, the grain size of the NbC coating is calculated from line broadening of XRD peaks using the Scherrer formula [28] after the correction for instrumental line broadening. As the results shown in Table 1, the calculated grain size obtained from different crystal planes range from 9.4 nm to 24.5 nm.

Fig. 2(a) and (b) show a typical cross-sectional SEM image of the as-deposited coating and an EDS spectrum acquired from the coating. The cross-sectional image reveals that the NbC coating, with a uniform thickness of ~15 μm, exhibits a homogeneous and compact microstructure which appears well bonded to the Ti-6Al-4V substrate. The composition of the coating, determined by EDS analysis (Fig. 2(b)), is equal to 54.1 at.% Nb and 45.9 at.% C, and the atomic ratio of Nb to C is slightly larger than that for the stoichiometric NbC. A plan-view bright-field TEM micrograph (Fig. 2(c)) taken from the NbC coating indicates that the coating comprises nanosized crystalline grains with an equiaxed shape with an average grain size of ~10 nm. The average grain size estimated by TEM observation is slightly smaller than the calculated value from the XRD data. As well known, the XRD data of a sample are recorded from the larger region and depth as compared to TEM. The
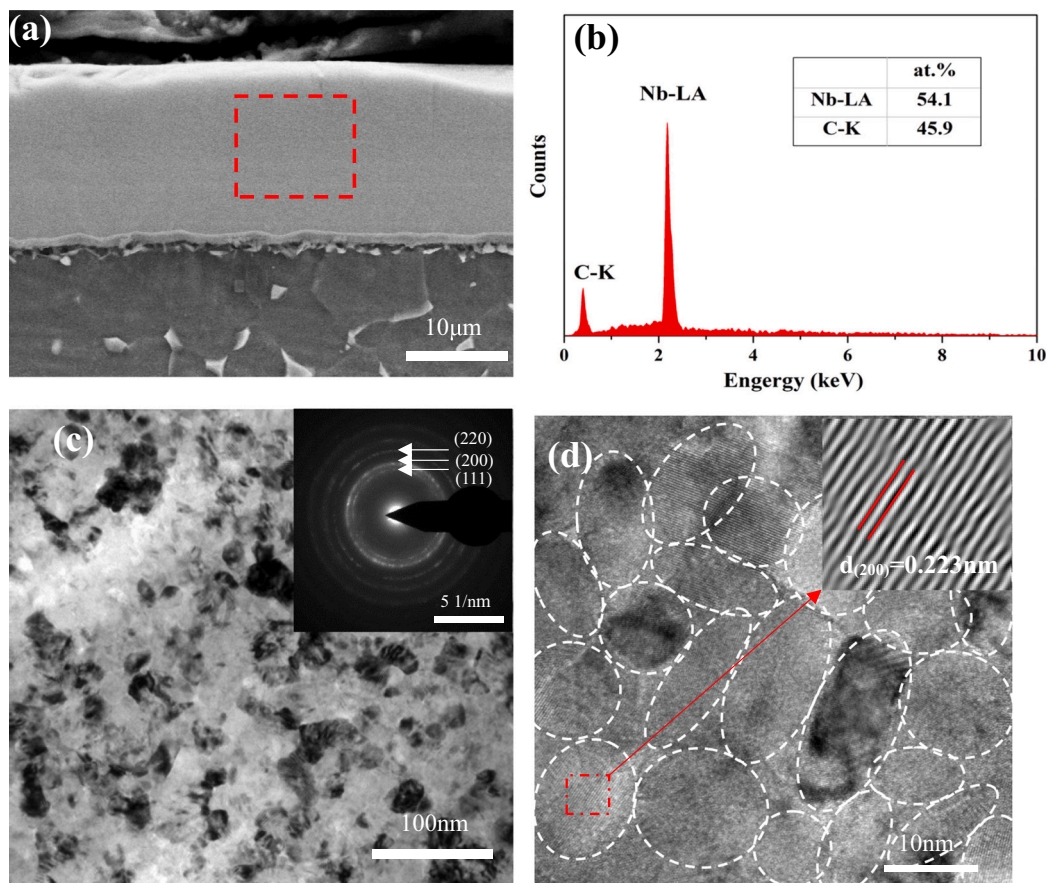
Fig. 2. (a) Cross-sectional SEM image of the as-deposited coating and (b) the corresponding EDS spectrum from the area marked with the red rectangle in (a). (c) Bright-field plan view TEM image of the NbC coating with, inset, selected area diffraction (SAD) pattern (d) high-resolution TEM image with, inset, showing the {200} planes of NbC.
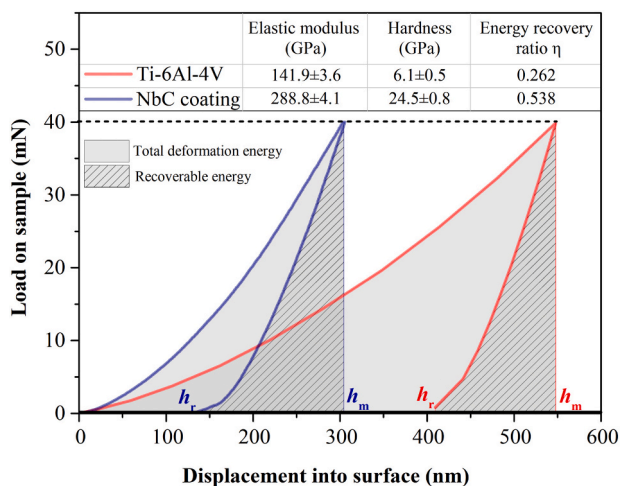

Fig. 3. Indentation load vs. indenter displacement (P-h) curves for NbC coated Ti-6Al-4V as well as uncoated Ti-6Al-4V obtained by nanoindentation to an applied maximum load of 40 mN.

differences in the average grain size between XRD and TEM data may be related to the uneven distribution of crystallite sizes in the NbC coating. The d-spacing values obtained from different diffraction rings shown in the selected area diffraction (SAD) pattern (inset in Fig. 2(c)) match well with the interplanar spacings for cubic δ-NbC phase. The high-resolution TEM (HRTEM) image (Fig. 2(d)) displays a well-defined lattice

separation of 2.23 Å, which is assigned to the interplanar distance for (200) planes in the cubic δ-NbC phase.

3.2. Mechanical characterization

Fig. 3 shows a typical indentation load versus indenter displacement (*P–h*) curves for NbC coated Ti-6Al-4V as well as uncoated Ti-6Al-4V alloy obtained by nanoindentation to an applied maximum load of 40 mN. It is clearly evident that the maximum penetration depth (h_m) and the residual impression depth(h_r) are significantly smaller for the NbC coating as compared with the uncoated substrate. This suggests that, under same load, the uncoated Ti-6Al-4V has experienced greater plastic deformation than the coating, in other words, the presence of the coating improves the resistance of Ti-6Al-4V to plastic deformation. Furthermore, elastoplasticity is a key parameter describing the ability of a material to absorb the energy of the collapsing bubbles under cavitation erosion conditions [29]. The elastoplasticity of a material is evaluated by the energy recovery ratio (η), i.e., the ratio of the recoverable energy (that is, the area under unloading curve) to the total deformation energy (that is, the area under loading curve). The η value for the coating is twice that of Ti-6Al-4V alloy, indicating that the elastoplasticity of the former is much larger than that of the latter.

Hardness (H) and elastic modulus (E) values for coated and uncoated Ti-6Al-4V extracted from *P–h* curves using Oliver-Pharr's analysis are shown in inserted table of Fig. 3. The H and E values increase significantly from 6.1 ± 0.5 GPa and 141.9 ± 3.6 GPa for uncoated Ti-6Al-4V to 24.5 ± 0.8 GPa and 288.8 ± 4.1 GPa for the coated Ti-6Al-4V. The hardness values of NbC$_x$ coatings are strongly dependent on carbon content and deposition technologies. For the binary Nb—C coating, the
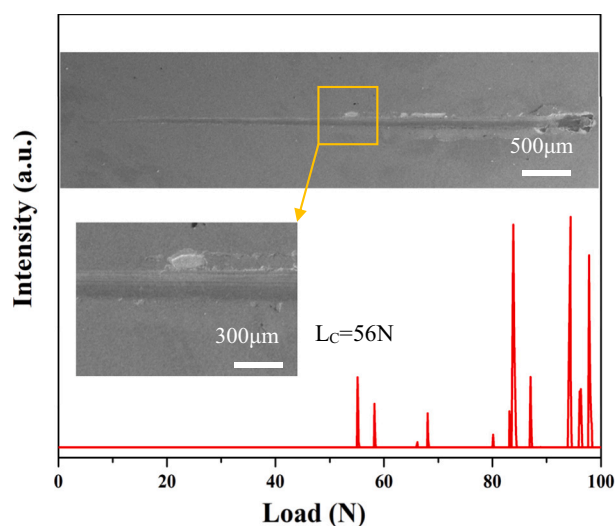
Fig. 4. Acoustic emission signal vs. normal load curve for the NbC coating together with secondary electron image of the scratch groove morphology.
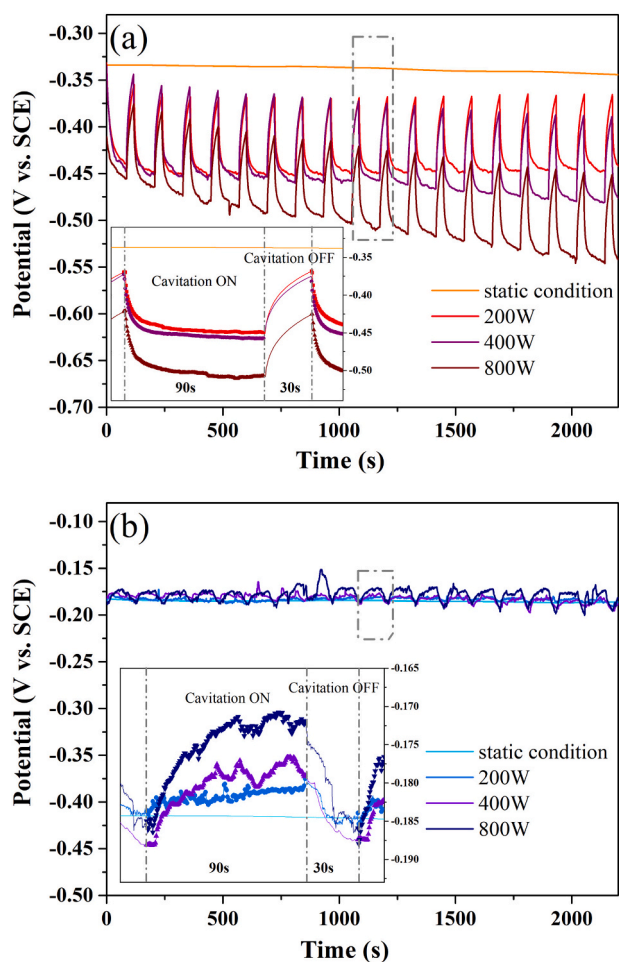

Fig. 5. EOCP vs. time plots for (a) the Ti-6Al-4V alloy and (b) the NbC coating under static and cyclic cavitation (alternating stagnant state for 30 s and cavitation state for 90 s at different output powers) conditions in a naturally aerated 3.5 wt% NaCl solution.

hardness values vary from 11.3 GPa to 25 GPa, which is closely correlated with phase structure, residual stress and grain size of these Nb—C coatings [13]. The hardness value of the NbC coated Ti-6Al-4V is very close to the upper limit of reported data. Some researchers suggested that the ratio between hardness and elastic modulus (H/E) can be used as an index of predicting the cavitation erosion resistance of a hard coating, namely, the higher H/E value, the higher the cavitation erosion resistance for a coating would be [30]. In light of this parameter, the NbC coating is expected to show a higher cavitation erosion resistance, because the H/E ratio of the coating (0.085) is larger than that of uncoated Ti-6Al-4V (0.043).

Under the action of micro-jet impingement, the repeated impact load introduces shear stresses at the coating/substrate interface, and so the coating may become partially spalled off when the cumulative shear stresses exceed the adhesion strength between the coating and the substrate. Krella et al. [31] reported that with increasing critical load for TiN coatings from 14 N to 30 N, the weight loss of the coatings was decreased and the incubation period was prolonged under cavitation conditions. Hence, good adhesion is indispensable to cavitation erosion resistance for a soft substrate–hard coating system. To determine the degree of adhesion of the NbC coating to the Ti-6Al-4V substrate, the critical load, where the first appearance of interfacial failure can be observed, was evaluated by scratch adhesion tests. Fig. 4 shows a typical acoustic emission signal against the normal load curve, together with a secondary electron image showing the scratch groove morphology. It is evident that the first evident acoustic emission signal is released at a normal load of 56 N, and the corresponding image of the scratch track indicates that large-scale delamination is observed at this load at the edge of the scratch track. This result suggests that the critical load (Lc) of the coating is ~56 N. This high adhesion strength for this NbC coating is likely to be beneficial in minimizing coating spallation during the cavitation erosion-corrosion process.

3.3. Electrochemical measurements

3.3.1. Effect of cavitation on the open circuit potential (E_{OCP})

Fig. 5 shows the E_{OCP} versus time plots for the coated and uncoated samples under static and cyclic-cavitation (that is, an alternating cavitation state for 90 s and stagnant state for 30 s) conditions in a naturally aerated 3.5 wt% NaCl solution. Under the static solution condition, the E_{OCP} value is more positive for the coating than that for the uncoated Ti-6Al-4V, meaning that ennoblement of the Ti-6Al-4V surface is achieved by coating with NbC. Under cyclic-cavitation conditions, when cavitation is turned on, the E_{OCP} for the uncoated Ti-6Al-4V shifts to more negative values and the decrease in the E_{OCP} values is accentuated with increasing output power, when the stagnant state is active, and the E_{OCP} values move back toward a noble direction. On the contrary, for the NbC coating, after commencing cavitation, the E_{OCP} goes further toward more positive values than that in the static solution and the E_{OCP} values increase with increasing output power; when cavitation is stopped, the E_{OCP} drops down to around the value obtained at in a static solution. During the cavitation process, the variations of E_{OCP} are generally attributed to two competing factors including detachment of the protective passive film and the increase of mass transfer of dissolved oxygen, because the stirring of the electrolyte, together with repetitive impacts of the collapsing bubble caused by vibration of the horn tip, occur simultaneously [32]. For uncoated Ti-6Al-4V, such a cathodic shift of E_{OCP} originates from the simultaneous actions of the erosive and corrosive processes, which activate the Ti-6Al-4V surface through removal of the surface protective film which accelerates the anodic reaction rate. This results in the formation of galvanic coupling between the mechanically depassivated region and the surrounding passive region. The protective oxide film is readily destroyed under a higher output power, and thus the diminution of the E_{OCP} is more accentuated with increased output power. Once the cavitation period is turned off, the Ti-6Al-4V surface repassivates rapidly and the E_{OCP} value switches to
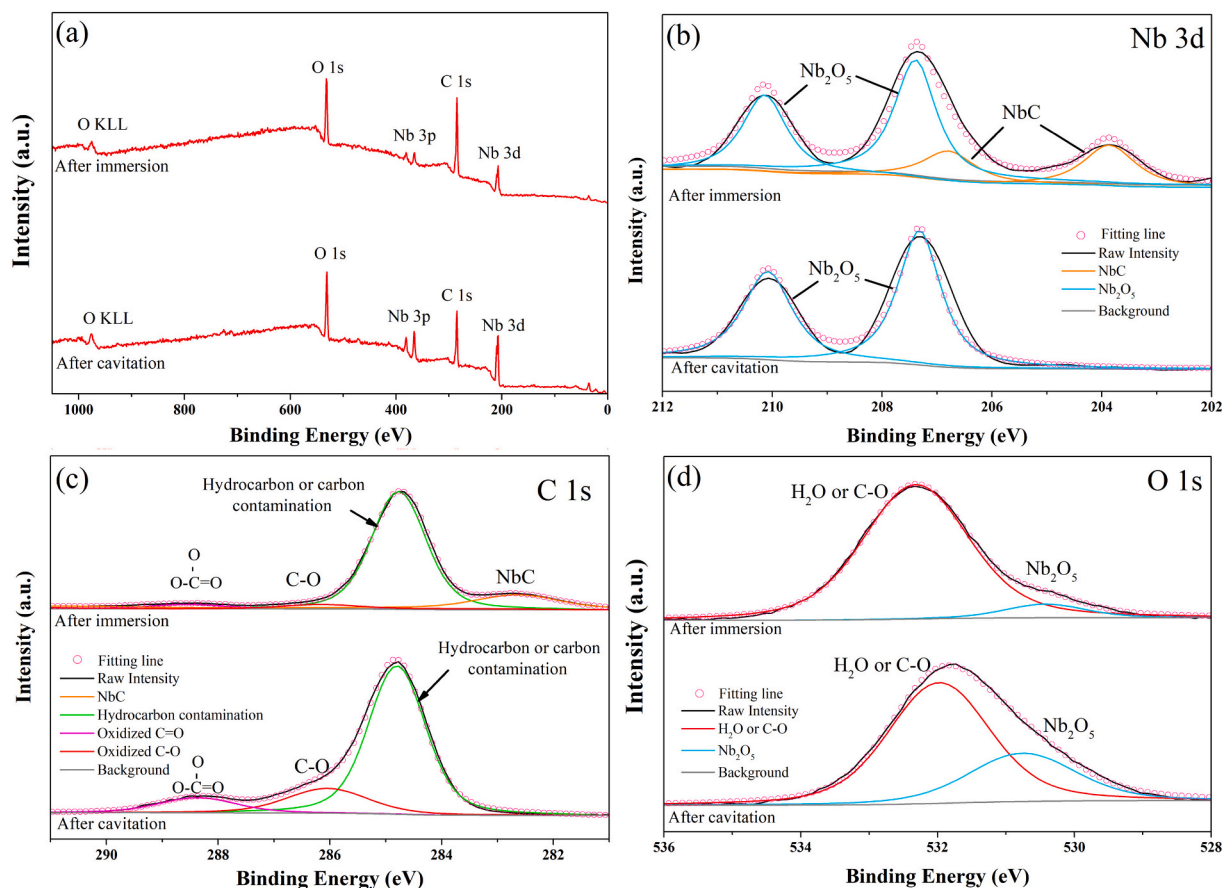
Fig. 6. (a) XPS survey spectra and the high-resolution XPS spectra for (b) Nb 3d, (c) C 1s and (d) O 1s peaks collected from the NbC coating under both static immersion and cavitation erosion conditions at an output power of 800 W in a 3.5 wt% NaCl solution for 6 h.

a positive direction. This characteristic in the E_{OCP} shift is also similar to that exhibited by a range of stainless steels exposed to a 3.5 wt% NaCl solution [3,19]. In contrast, for the NbC coating, the noble shift in E_{OCP} for the coating under cavitation conditions is dominated by the mass transfer of oxygen. The dissolved oxygen in solution is neutralized through the cathodic reaction (oxygen reduction reaction) occurring on the coating and the required electrons of this reduction reaction are provided by the anodic oxidation reaction, thereby leading to a rise in the E_{OCP} value. In the stagnant state, the corrosion reaction rate decelerates due to a reduction in oxygen, thus causing the E_{OCP} value to drift in a negative direction. Furthermore, with increasing output power, the transport rate of oxygen increases and hence the positive shift in the E_{OCP} is more pronounced. Such changes in potential are similar to that of some alloys or thermal spray coatings exposed to NaCl-based solutions [12,33]. Unlike the uncoated Ti-6Al-4V, the E_{OCP} of the coating fluctuates, within a very narrow range, around the level of that for the static solution. This suggests that the passive film formed on uncoated Ti-6Al-4V is easily removed and much less protective than that grown on the coating under cyclic-cavitation conditions in a 3.5 wt% NaCl solution.

3.3.2. XPS analysis

As is well known, the protectiveness of a passive film is associated with its chemical composition, stability, structure and adherence, which play an important role in the resistance of a material to attack by cavitation erosion-corrosion. Previous work has shown that the chemical composition [34] and thickness [35] of the passive film formed on stainless steels under cavitation conditions were different from those of passive films produced in the absence of the cavitation. To unravel the changes in the elemental composition and chemical state of the passive film after ultrasonic cavitation tests, XPS analysis was performed on the

NbC coating under both static conditions and cavitation erosion at an output power of 800 W in a 3.5 wt% NaCl solution for 6 h. As shown in Fig. 6(a), the XPS survey spectra obtained from the two samples comprise the Nb 3d, Nb 3p, O 1s and C 1s peaks. From the deconvoluted XPS spectra for Nb 3d (Fig. 6(b)), two sets of spin-orbit doublets for Nb $3d_{5/2}$ and Nb $3d_{3/2}$ are observed for the non-cavitated coating, among which the Nb $3d_{5/2}$ peaks, located at binding energies of 203.25 eV and 207.3 eV, correspond to the presence of NbC and Nb_2O_5, respectively [36,37]. However, the XPS spectrum for Nb 3d collected from the cavitated coating shows no peak associated with NbC; only a doublet peaks assigned to Nb_2O_5 was identified. This suggests that a thinner passive film is grown on the non-cavitated coating, because the measured NbC peak derives from the coating underlying the passive film. As can be seen from Fig. 6(c), the C 1s XPS spectrum for the non-cavitated coating can be deconvoluted into four components. The peaks recorded at binding energies of 282.5, 284.6, 286.2 and 288.6 eV can be attributed to Nb—C bonds in NbC, surface hydrocarbon contamination, oxidized C—O and C=O, respectively [38–40]. The presence of the C—O and C=O species results from the products of oxidation of the carbide. As expected, no peak corresponding to Nb—C bonds was detected for the coating after cavitation of 6 h, which is consistent with the analysis of the Nb 3d XPS spectrum under these conditions. The deconvoluted O1s core level spectra (Fig. 6(d)) for the NbC coating with, or without, cavitation consists of an intense peak located at 532.5 eV corresponding to adsorbed water or carbon-to-oxygen bonding (such as C—O and C=O bonds), and a weaker peak located at 529.8 eV originating from Nb_2O_5 [41]. However, the peak intensity corresponding to Nb_2O_5 is stronger for the cavitated coating than for the non-cavitated coating. This offers further evidence of the formation of a thicker passive film on the cavitated coating. The above
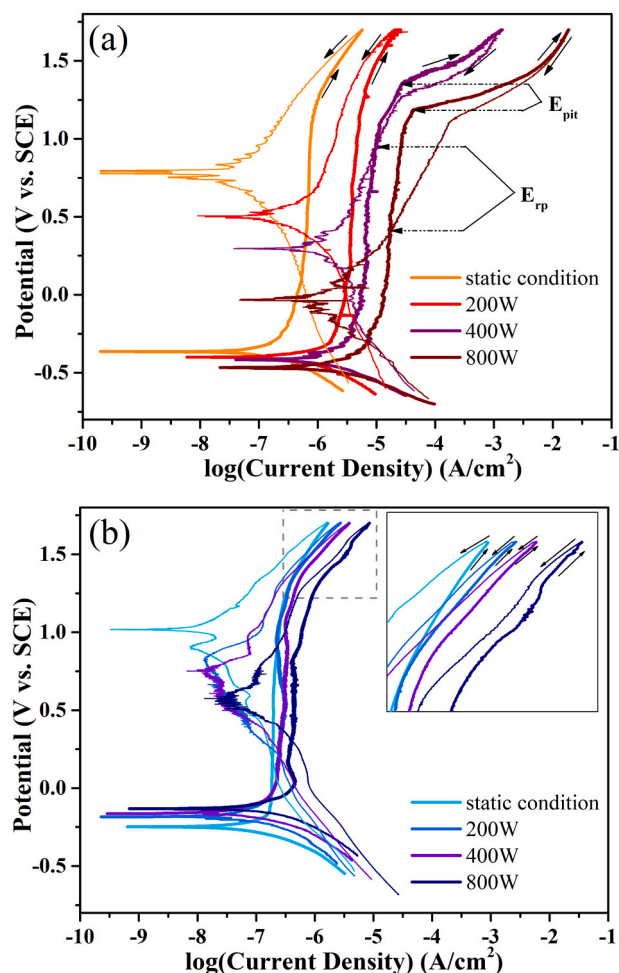
Fig. 7. The potentiodynamic cyclic polarization curves for (a) uncoated Ti-6Al-4V and (b) the NbC coating in a 3.5 wt% NaCl solution under static conditions and the cavitation erosion conditions at different output powers. The potentiodynamic cyclic polarization measurements were carried out after an exposure time of 6 h in a 3.5 wt% NaCl solution under static electrolyte and cavitation conditions.

Table 2
Electrochemical parameters for the uncoated Ti-6Al-4V and the NbC coating obtained from the potentiodynamic polarization curves.

	Cavitation output power	E_{corr} (V_{SCE})	i_{corr} $(A\,cm^{-2})$
Ti-6Al-4V	Static condition	−0.364	7.18×10^{-7}
	200 W	−0.399	2.14×10^{-6}
	400 W	−0.416	5.81×10^{-6}
	800 W	−0.466	9.72×10^{-6}
NbC coating	Static condition	−0.248	1.16×10^{-7}
	200 W	−0.185	1.38×10^{-7}
	400 W	−0.164	1.83×10^{-7}
	800 W	−0.132	2.30×10^{-7}

XPS analysis demonstrates that under cavitation conditions an increase in oxygen transfer accelerates both the cathodic and anodic reaction rates, leading to thickening of the passive film on the cavitated coating.

3.3.3. Potentiodynamic cyclic polarization tests

To reveal the susceptibility of the NbC coating to pitting corrosion in a chloride ion-containing aqueous solution under ultrasonic cavitation conditions, potentiodynamic cyclic polarization measurements were conducted on the coating at different applied output powers in a 3.5 wt

% NaCl solution. The potentiodynamic cyclic polarization plots of uncoated and NbC-coated Ti-6Al-4V are plotted in Fig. 7, where the solid arrows indicate the potential scan direction. The corresponding corrosion kinetic parameters extracted from the forward potential scanning plots, including corrosion potential (E_{corr}) and corrosion current density (i_{corr}), are presented in Table 2. For comparison, the potentiodynamic cyclic polarization plots of the two samples in a 3.5 wt% NaCl solution under quiescence conditions are also presented. As shown in Fig. 7, as the applied output power increased from 0 to 800 W, the E_{corr} values of the coating increased from −0.248 V to −0.132 V, whereas the E_{corr} values for the uncoated Ti–Al–4V alloy decreased from −0.364 V to −0.466 V. This variation of the E_{corr} values with the applied output powers is also consistent with the trend observed in the E_{OCP} versus time plots. In a quiescent 3.5 wt% NaCl solution, the i_{corr} values of both the samples are very small, of the order of $10^{-7} A/cm^2$. However, after the onset of cavitation, the i_{corr} values increase with the applied output power, but the extent of the increase differs largely between the two samples. At an output power of 800 W, there was a 2-fold increase for the coating and a 10-fold increase for uncoated Ti-6Al-4V in the i_{corr} values as compared to their respective values obtained in a quiescent solution. At the same output power, the coating exhibits a higher E_{corr} value and a lower i_{corr} value than uncoated Ti-6Al-4V, suggesting significant improvement in cavitation erosion-corrosion resistance of the Ti-6Al-4V alloy through coating with NbC. At output power levels below 200 W, the uncoated Ti-6Al-4V shows lower current density values during the reverse potential scan compared to the forward potential scan, that is, the formation of a negative hysteresis loop in the plot, indicating the absence of pitting corrosion on the Ti-6Al-4V alloy surface even up to an anodic potential as high as +1.7 V. However, at output powers greater than 200 W, a pitting potential (E_{pit}), defined as a potential above which current density increases abruptly, was visible in anodic branches during the forward potential scan. Moreover, when the potential is swept toward the reverse direction, the decrease in current density value means that the forward and reverse scan curves intersect at E_{rp} (defined as the repassivated potential), resulting in the formation of a positive hysteresis loop in the cyclic polarization plots. At potentials lower than E_{rp}, re-passivation of pits that have formed occurs. Generally, the size of the hysteresis loop reflects re-passivation ability of a material, namely, the smaller the positive hysteresis loop, the easier the re-passivation process [42]. It is evident from Fig. 7(a) that with an increase in the output power from 400 W to 800 W, the hysteresis loops become larger in magnitude, implying that the increased intensity of cavitation lowers the re-passivation ability of bare Ti-6Al-4V. In contrast, no hysteresis loop was observed for the NbC coating, even at output power of 800 W, denoting that the coating has excellent pitting corrosion resistance under ultrasonic cavitation conditions.

3.4. Electrochemical noise study

3.4.1. Noise analysis in time domain

To gain further insight into the impact of cavitation conditions on the extent of passive film rupture and repassivation for this coating, electrochemical noise measurements were carried out after an exposure time of 6 h in a 3.5 wt% NaCl solution under both static electrolyte and cavitation conditions. Fig. 8 compares the typical electrochemical current and potential noise measurements over a period of 1000 s for both the NbC coated and uncoated substrate exposed to a 3.5 wt% NaCl solution. Fig. 8(a) shows the amplitude of the current fluctuation peaks for bare Ti-6Al-4V rises by two orders of magnitude with an increase in output power from 0 W (static electrolyte) to 800 W. A significant increase in the electrochemical current noise level suggests that the increased intensity of cavitation renders the bare Ti-6Al-4V surface more electrochemically active and hence accelerates the electrochemical reaction rate occurring at the solution/bare Ti-6Al-4V interface. Of note, the largest increases in the intensity of current noise level were observed as the output power increased from 200 W to 400 W, suggesting that
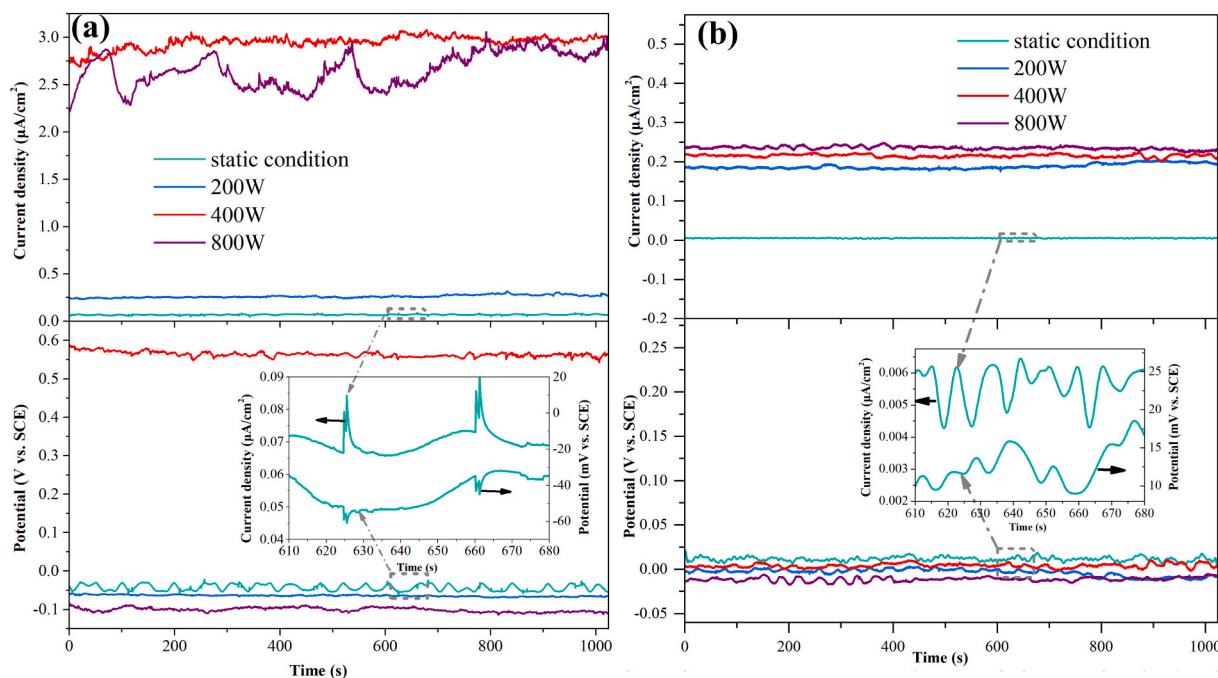
Fig. 8. Electrochemistry current and potential noise records for (a) the uncoated Ti-6Al-4V and (b) the NbC coating after an exposure time of 6 h in a 3.5 wt% NaCl solution under static conditions and cavitation erosion conditions at different output powers.
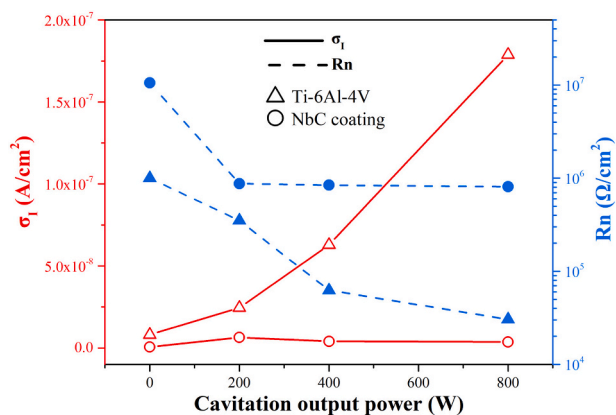

Fig. 9. Rn and σI values of the NbC coated and uncoated Ti-6Al-4V as a function of cavitation output power under quiescent and ultrasonic cavitation conditions.

there is a threshold value between these two output powers. Above this threshold value, it is suggested that the generated microjets and shockwaves have sufficient kinetic energy to cause rupture of the passive film grown on uncoated Ti-6Al-4V. In addition, bare Ti-6Al-4V exhibits pronounced potential and current fluctuations in a static 3.5 wt% NaCl solution. As shown in the magnified portion of the noise signal (inset in Fig. 8(a)), the potential and current always fluctuate simultaneously in opposite directions, and some spikes of current and potential, characterized as a sudden rise in current (or an abrupt decrease of potential) followed by sharp drop to original value (or a quick increase of potential), are observed. Such a noise pattern may be associated with the dissolution/breakdown and repair of the local passive films on bare Ti-6Al-4V [43]. On the contrary, for the NbC coating (as shown in Fig. 8 (b)), regardless of whether the coating is exposed under static electrolyte

or cavitation conditions, the potential and current transients are of much higher frequency than the equivalent signals detected for bare Ti-6Al-4V and the amplitude of current and potential oscillations are 1 nA and 20 mV, respectively, which are independent of the applied output power. EN transients with high frequency and of low intensity indicate that the coating is maintained in a passive state under both static electrolyte and cavitation conditions.

The amplitude of random current and potential noise signal in the time domain can be described by the standard statistical parameters, including the standard deviations current (σ_I) and potential (σ_V) fluctuations [44]. The standard deviation ratio of σ_V to σ_I, defined as noise resistance (R_n), shows a good correlation with the values of polarization resistance (R_p) and the charge transfer resistance (R_{ct}) derived from the potentiodynamic polarization and electrochemical impedance spectroscopy (EIS) measurements, respectively [45]. Fig. 9 shows the R_n and σ_I values for the NbC coated and uncoated Ti-6Al-4V substrate under quiescent and ultrasonic cavitation conditions. As shown in Fig. 9, the σ_I values for bare Ti-6Al-4V are found to increase linearly with output power, from 1.01×10^{-8} under a static electrolyte to 1.79×10^{-7} at an output power of 800 W. In contrast, the σ_I values for the NbC coating remain almost constant, about of the order of 10^{-9}, even with an increase in the output power. This indicates that with increases in the intensity of the cavitation conditions, the corrosion activity of uncoated Ti-6Al-4V increases markedly, but the NbC coating maintains a low corrosion activity that is insensitive to the applied output powers. The calculated R_n values for uncoated Ti-6Al-4V decrease by about two orders of magnitude from $1.00 \times 10^6 \ \Omega cm^2$ under quiescent conditions to $3.04 \times 10^4 \ \Omega \ cm^2$ at an output power of 800 W. For the NbC coating, the calculated R_n value is $1.06 \times 10^7 \ \Omega \ cm^2$ under quiescent condition, but under ultrasonic cavitation conditions it is not significantly changed with increasing output power to a value of around $8.5 \times 10^6 \ \Omega \ cm^2$, at an output power of 800 W, which is two orders of magnitude larger than that for the Ti-6Al-4V substrate. Higher R_n values indicate a lower corrosion rate for the coating under both a static electrolyte and
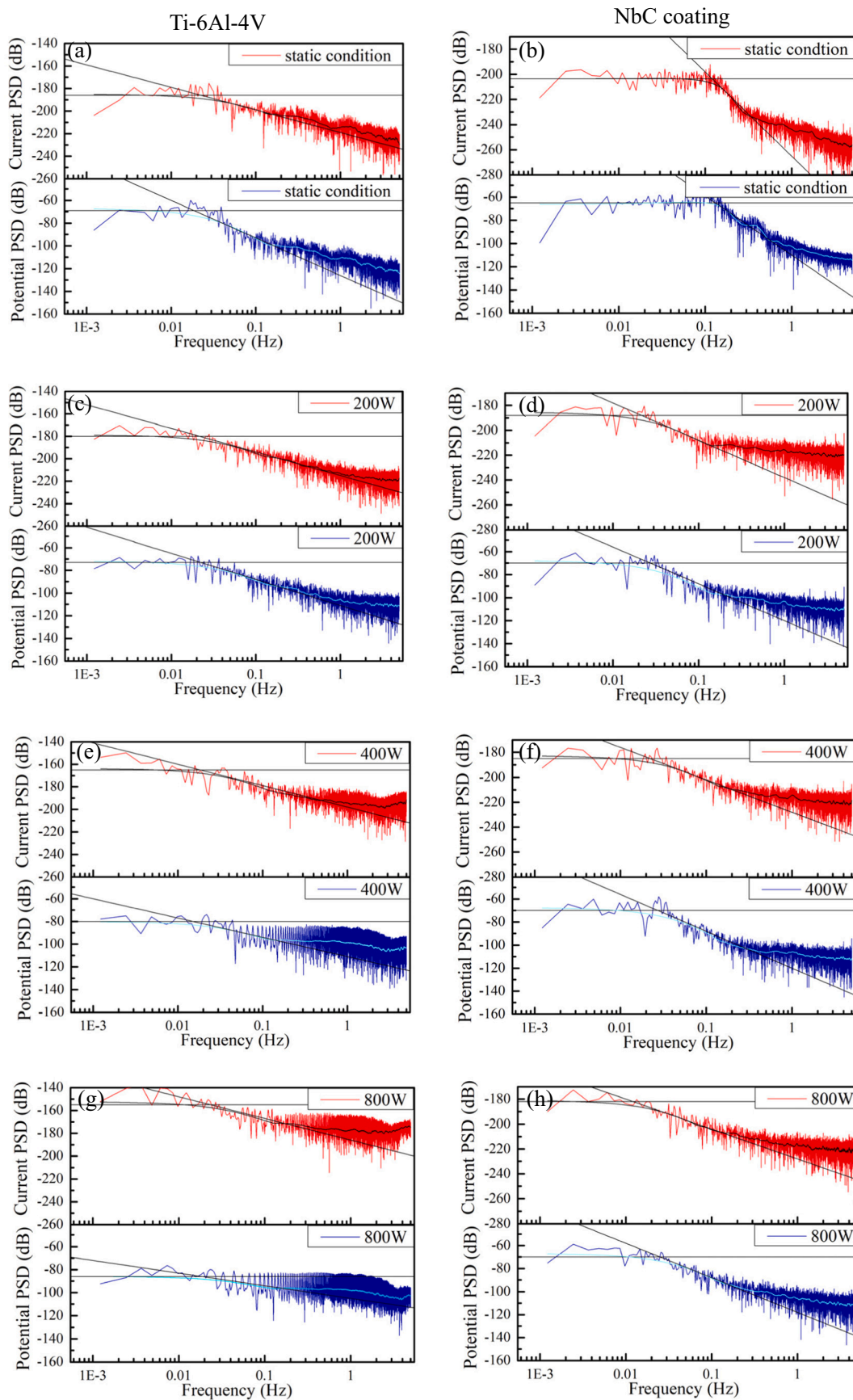
Fig. 10. Typical electrochemical current and potential noise PSD plots on a log-log scale taken from (a, c, e and g) uncoated Ti-6Al-4V and (b, d, f and h) the NbC coating after exposure time of 6 h in a 3.5 wt% NaCl solution under (a and b) static conditions and cavitation conditions at output power levels of (c and d) 200 W, (e and f) 400 W and (g and h) 800 W, respectively.

Table 3

Electrochemical noise data derived from the electrochemical noise power spectrum for the uncoated Ti-6Al-4V and the NbC coating in a 3.5 wt% NaCl solution under static conditions and the cavitation erosion conditions with different output power levels.

		W_E dB	k_E dB/decade	W_I dB	k_I dB/decade
Ti-6Al-4V	Static condition	−69	−33	−186	−27
	200 W	−73	−23	−180	−21
	400 W	−80	−17	−165	−18
	800 W	−86	−11	−155	−17
NbC coating	Static condition	−65	−51	−204	−67
	200 W	−70	−32	−187	−30
	400 W	−70	−32	−185	−26
	800 W	−70	−30	−183	−24

cavitation conditions.

3.4.2. Noise analysis in frequency domain

At times, the recorded potential or current transient events may occur at virtually the same time, and the time intervals between those transient events is so short that the transient peaks are severely strained and overlapped in time domain due to mutual interference. Under these circumstances, there is a significant advantage in converting the EN data from the time domain to the frequency domain by applying mathematical procedures (e.g., a fast Fourier transform (FFT)). Frequency domain analysis not only enables us to distinguish the different types of corrosion process in operation and to predict the dominant corrosion mechanisms, but also to quantitatively estimate the intensity of corrosion [46]. In this work, the frequency–dependent current and potential power spectra density (PSD) analysis was performed using FFT transformation and the Hanning's window function is applied to minimize

artifacts in the spectra. Fig. 10 shows current and potential PSD plots on a log-log scale taken from both the NbC coating and bare Ti-6Al-4V after exposure for 6 h in 3.5 wt% NaCl solution under both static electrolyte and cavitation conditions. It is clear that all the PSD plots are characteristic of two sections, each with a different slope over the whole working frequency range: an approximate horizontal jagged line in the lower frequency region, namely a white noise section; in the higher frequency region, the PSD value decreases continuously with frequency, namely a $f^{-\alpha}$ noise section. The frequency at cross point between white noise and $f^{-\alpha}$ noise is defined as the roll-off frequency (f_c) [47]. Two important parameters associated with the corrosion kinetics, including plateau amplitude in low frequency region or white noise level (W_I for the current noise and W_E for the potential noise) and the slope of high frequency linear region (the roll-off slope, k), can be extracted from these PSD plots and these are summarized in Table 3. From Table 3, with increasing output powers from 0 W (stationary solution) to 800 W, the W_I values increase and the W_E values decrease for both NbC coated and uncoated Ti-6Al-4V. Whether in a static electrolyte or at a given output power, the W_I value for the coating is considerably smaller than that for bare Ti-6Al-4V, suggesting that the coating possesses a lower corrosion rate. The changing trend of W_I with output power resembles the variation of σ_I values with output power, implying a good correlation between the current PSD and σ_I values. The roll-off slopes (k values) for current and potential PSD plots can be used as a valuable indicator to discern whether a specific mode of corrosion process is general or localized corrosion. As a general trend, if the roll-off slope is larger than −20 dB/decade, then pitting corrosion is dominant (or for values small than −20 dB/decade general corrosion dominate) [48]. For uncoated Ti-6Al-4V, the k values for current and potential PSD increase with output power, and when the output power is greater than 400 W, the k values are higher than −20 dB/decade. This suggests that the passive film
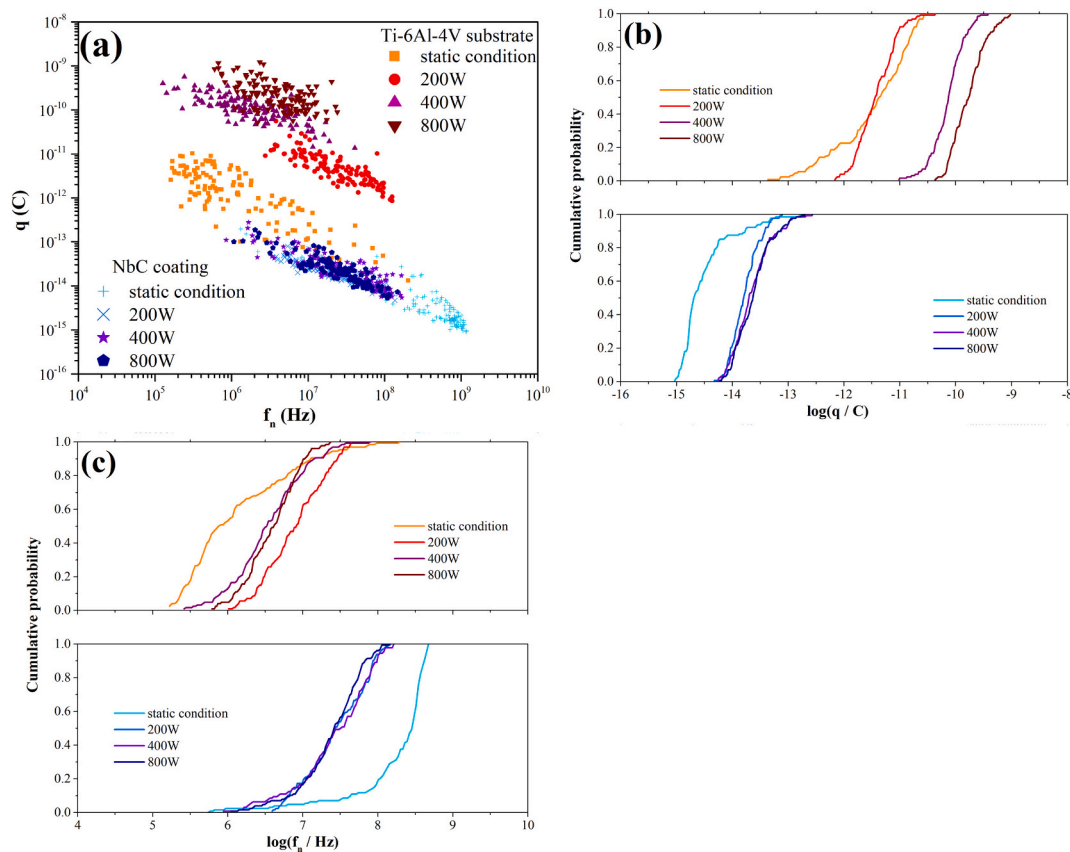

Fig. 11. (a) q vs. f_n plot and the cumulative probability plots of (b) q and (c) f_n for the uncoated Ti-6Al-4V and the NbC coating after an exposure time of 6 h in a 3.5 wt% NaCl solution under static conditions and cavitation erosion conditions at different output powers.

grown on uncoated Ti-6Al-4V becomes more unstable with increasing output power and pitting corrosion initiates at output powers of 400 W or more. Although the k values of current and potential PSD for the NbC coating also increase with increasing output power, the k values are always less than -20 dB/decade even at an output power of 800 W. This result suggests that the coating can stabilize the passive state under both stationary and cavitation conditions. These results are consistent with the potentiodynamic cyclic polarization analyses.

3.4.3. Shot noise theory analysis

As a statistical method of the EN signals, the shot noise analysis is further employed to investigate the nature of the corrosion processes under cavitation conditions by assuming that current noise consists of independent charge packets with a short duration for an individual packet in the frequency domain [49]. On the basis of shot noise theory, two parameters of interest: average charge (q) in each event and the corrosion event frequency (f_n), can be determined using the following Eqs. (2) and (3) [50]:

$$q = \frac{\sqrt{\Psi_E}\sqrt{\Psi_I}}{B} = \frac{\sigma_V \sigma_I}{Bb} \tag{2}$$

$$f_n = \frac{B^2}{\Psi_E A} = \frac{B^2 b}{\sigma_V^2} \tag{3}$$

where Ψ_E and Ψ_I are the low frequency PSD values of the potential and current noise in the power density spectra respectively, σ_I and σ_V are the standard deviation of current and potential respectively, A is the surface area of the working electrode, b is the bandwidth of measurement and B is the Stern-Geary coefficient [20]. Subsequently, the cumulative probability of f_n (F(f_n) and q(F(q)) are estimated from the set of 128 f_n and q data by using mean rank approximation. Fig. 11(a) shows the q versus f_n plots of the coating and bare Ti-6Al-4V after 6 h exposure in 3.5 wt% NaCl solution under static electrolyte and cavitation conditions. It is apparent that both the f_n and q values for the two samples have not fallen in the same order of magnitude, and in comparison with uncoated Ti-6Al-4V, the q versus f_n plots of the coating shift toward the region of lower q and higher f_n values. From the viewpoint of the shot noise analysis, the higher q value means more charge transferred in each event and, thus, the higher corrosion activity of the system, while the lower f_n value tends to promote more localized corrosion [51]. By combining a lower q value with higher f_n value, the NbC coating has a lower propensity for pitting corrosion than uncoated Ti-6Al-4V under both static and cavitation conditions. Fig. 11(b) and (c) present the calculated cumulative probability plots for q and f_n for the NbC coating and bare Ti-6Al-4V after 6 h exposure in a 3.5 wt% NaCl solution under static electrolyte and cavitation conditions. For uncoated Ti-6Al-4V, most f_n values are located between 10^5 and 10^8 Hz and most q values are of the order of 10^{-13}– 10^{-9}C. With increasing output power, most q values for bare Ti-6Al-4V increase, and when the output power increases from 200 to 400 W, the more pronounced increase of q values was observed. Meanwhile the f_n values decreased concurrently, indicating that uncoated Ti-6Al-4V appeared to be more susceptible to localized corrosion attack at output power values of 400 W and above. In the case of the NbC coating, for static conditions the q values lie in the range of 10^{-15}– 10^{-14}C and the f_n values are between 10^7 and 10^9 Hz. Meanwhile, under cavitation conditions, the cumulative probability plots of q and f_n almost overlapped, where the q values range between 10^{-14} and 10^{-13}C and the f_n values are approximately 10^6– 10^8 Hz. This suggests that both the corrosion rate and type of dominant corrosion process for the coating do not vary with the magnitude of output powers used in this work, which is accordance with the noise analysis in both the time frequency

Table 4
The frequency and timescale ranges for each crystal.

Crystal	Frequency range/Hz	Timescale range/s
D_1	10–5	0.1–0.2
D_2	5–2.5	0.2–0.4
D_3	2.5–1.25	0.4–0.8
D_4	1.25–0.625	0.8–1.6
D_5	0.625–0.3125	1.6–3.2
D_6	0.3125–0.15625	3.2–6.4
D_7	0.15625–0.078125	6.4–12.8
D_8	0.078125–0.0390625	12.8–25.6

domains. With the presence of NbC coating, the distribution of f_n shifts to a higher frequency region and simultaneously, the upper limit of the q values is dropped by four-fold under cavitation conditions, indicating an excellent protection afforded by the NbC coating.

3.4.4. Wavelet analysis

To compensate for the limitation in conventional Fourier analysis with respect to processing non-stationary noise signals (e.g., the direct current offset or transient noise peaks), wavelet transform, as a multi-resolution analytical procedure, has been employed to investigate transients in signal or precise time-scale analysis [52]. To further discriminate between the underlying various electrochemical corrosion events occurring during the cavitation process, the electrochemical current noise (ECN) records recorded from both the NbC coated and uncoated Ti-6Al-4V after 6 h exposure in a 3.5 wt% NaCl solution under static electrolyte and cavitation conditions were analyzed using a discrete wavelet transform (DWT). ECN data were decomposed into both a smooth coefficient (s_8) and detail coefficients ($d_j = d_1$ up to d_8) by using the orthogonal Daubechies wavelets of the fourth order (db4). The detail coefficients (d_1 to d_8) and the smooth coefficient (s_8) are also called the d series crystals and a S_8 crystal, respectively. More detailed description of the DWT method can be found elsewhere [53]. The timescale (time constant) ranges and the corresponding frequency ranges for the d series crystals are given in Table 4. To estimate the contribution of each level to the overall signal, the energy of each crystal (E_j) was calculated [54].

The detail (d_1 up to d_8) and smooth (s_8) wavelet coefficients obtained from signal decomposition of the current noise signals for uncoated Ti-6Al-4V and the NbC coating are shown in Figs. 12 and 13, respectively. The energy distribution plots (EDPs) corresponding to the current noise signals (shown at the top of Figs. 12 and 13), defined as the calculated energy of each crystal versus the crystal name plots, are shown in Fig. 14. It is worth noting that the energy distribution plots subtract the contribution of the S_8 crystal from the entire signal energy, because it is too large to shelter the contribution of the d series crystals. For bare Ti-6Al-4V, under both static solution conditions and a cavitation output power of 200 W (shown in Fig. 12 (a) and (b)), all the energies in the d series coefficients are weak and the energy is mainly concentrated on crystals d_1 up to d_4, indicating that the corrosion events that occurred in both cases are mainly dominated by small timescale process, such as the initiation of pit nucleation [55]. At higher output powers (400 and 800 W), the plot of each order d crystal fluctuates more frequently over large amplitudes, implying a marked increase in the intensity of the electrochemical event over the full timescale range. Meanwhile, it can be seen from Fig. 14 (a) that for a given detail coefficient, the energy increases with the output power and, for a given output power, the energy of the d series coefficients increases with increasing time scales (level j values) and the energy of detail coefficient d_8 has the largest contribution. The d_8 crystal corresponds to corrosion events with longer time-scales (i.e. a
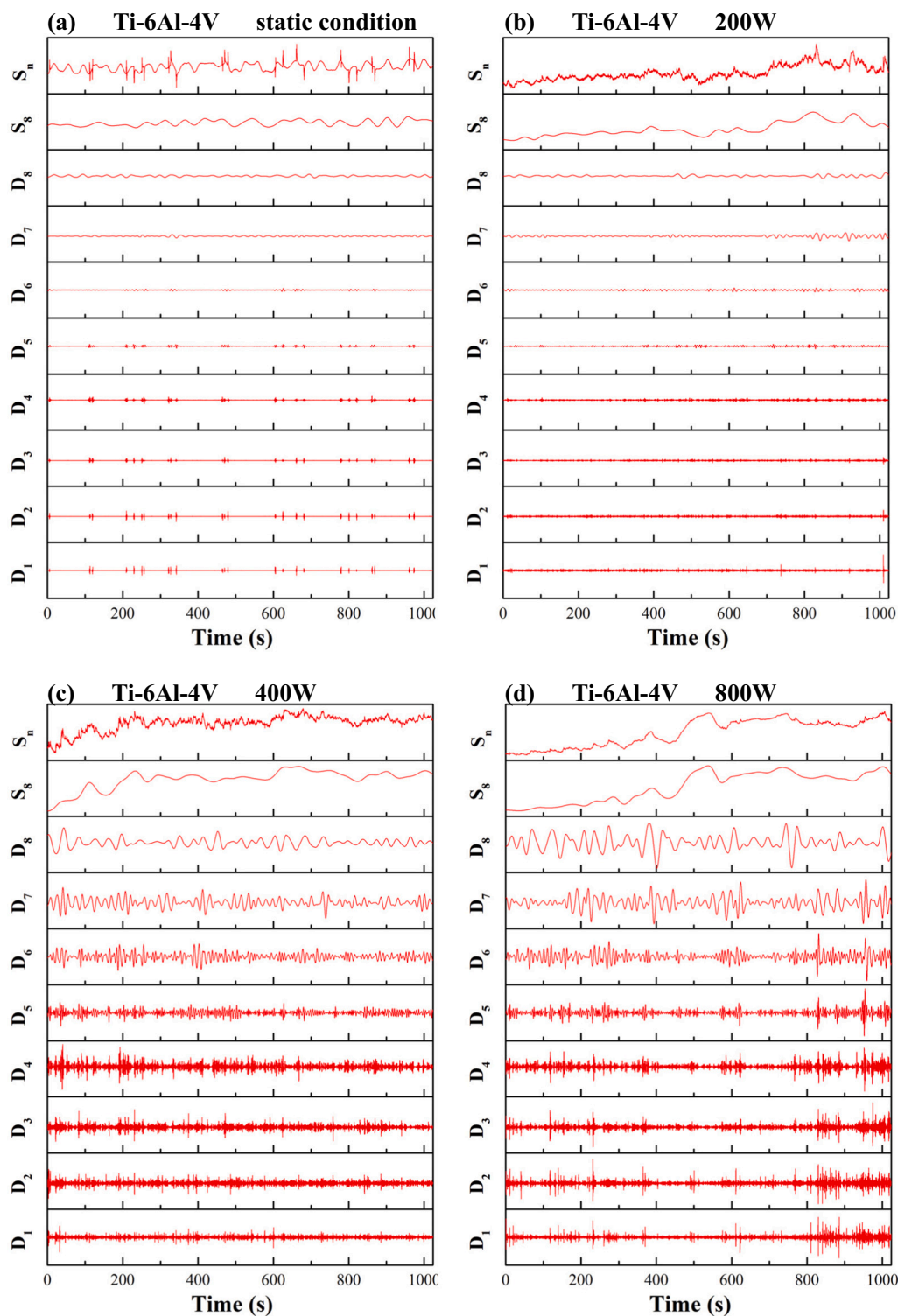
Fig. 12. Detail (D_1 up to D_8) and smooth (S_8) crystals of the electrochemical current noise signals (S_n) for the uncoated Ti-6Al-4V after an exposure time of 6 h in a 3.5 wt% NaCl solution under (a) static conditions and cavitation erosion conditions at output power levels of (b) 200 W, (c) 400 W and (d) 800 W, respectively.

time constant between 12.8 and 25.6 s), which may be related to oxygen diffusion [56]. Therefore, with increasing output power, the predominant corrosion process is controlled by the diffusion of oxygen and uncoated Ti-6Al-4V suffers more active corrosion. In the case of the NbC coating (shown in Fig. 13), there is no obvious difference in amplitude of local fluctuation for wavelet coefficients from d_1 to d_7 under both static solution and cavitation conditions, but the amplitude of the fluctuation for d_8 crystal increases with the output power. This is also shown by the

contribution of the d_8 crystal to the most of energy in all the d series coefficients (as shown in Fig. 14 (b)), indicating that the oxygen diffusion process prevails over other steps during the cavitation corrosion-erosion process. However, compared with bare Ti-6Al-4V, the total energy accumulated in the d series crystals for the coating is reduced by two orders of magnitude, suggesting a decrease in the activity of the electrochemical events.
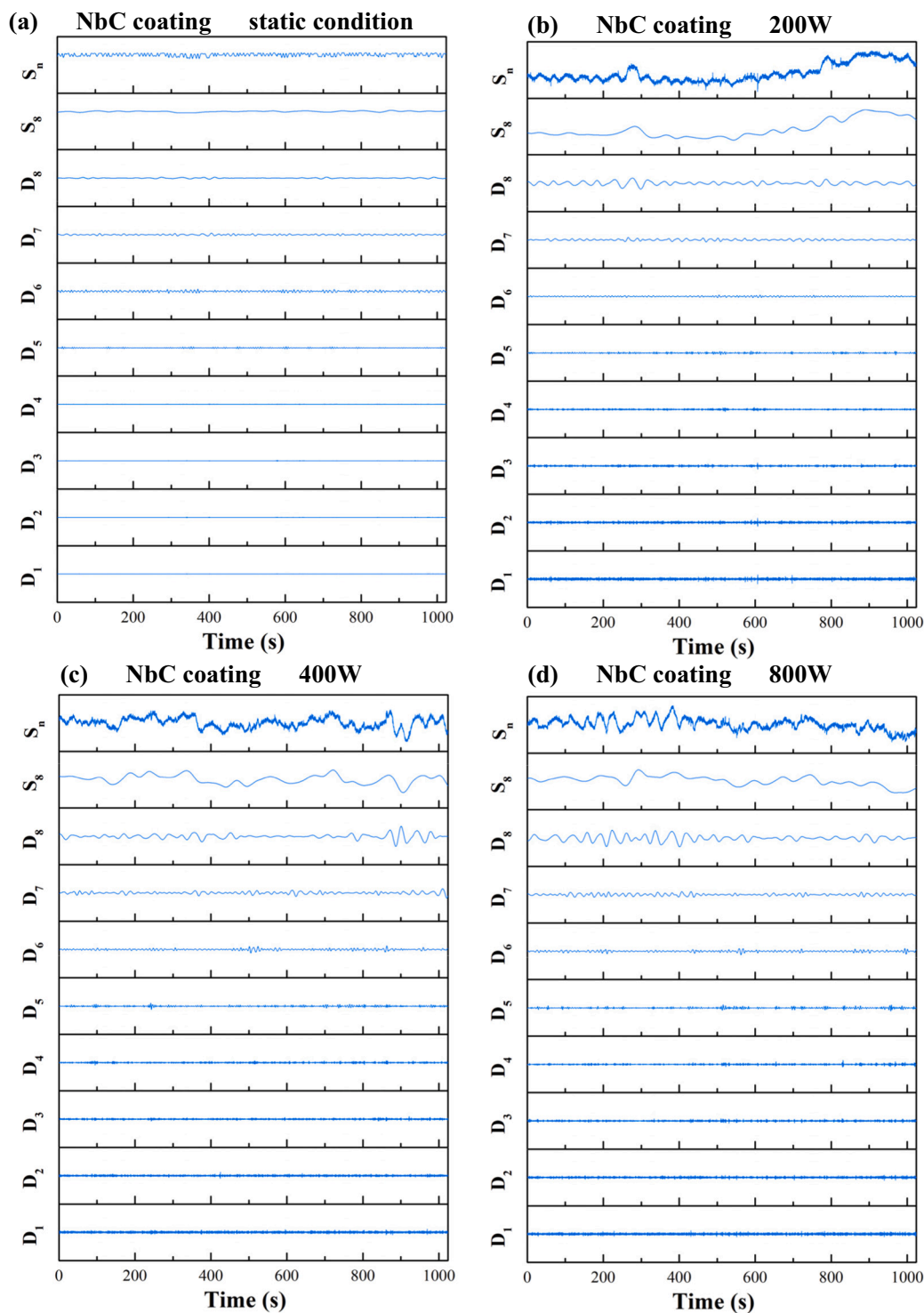
Fig. 13. Detail (D$_1$ up to D$_8$) and smooth (S$_8$) crystals of the electrochemical current noise signals (S$_n$) for the NbC coating after an exposure time of 6 h in a 3.5 wt% NaCl solution under (a) static conditions and cavitation erosion conditions at output power levels of (b) 200 W, (c) 400 W and (d) 800 W, respectively.

3.5. Corrosion surface observation

To further understand the results of these electrochemical tests, the changes in surface morphologies of the coated and uncoated Ti-6Al-4V alloy after 6 h exposure in a 3.5 wt% NaCl solution under static electrolyte and cavitation conditions are shown in Fig. 15. It is evident in Fig. 15 (a) and (b) that the surfaces of both the coated and uncoated

substrate appear smooth and featureless after soaking for 6 h in static 3.5 wt% NaCl solution, indicating that both samples exhibit good corrosion resistance in this solution. At an output power of 200 W (Fig. 15(c)), a large proportion of the Ti-6Al-4V surface area remains unchanged, except for the presence of some pinholes. In this case, the activation-controlled processes with small timescales, such as the initiation/repassivation of metastable pitting, mainly occur on the Ti-6Al-4V
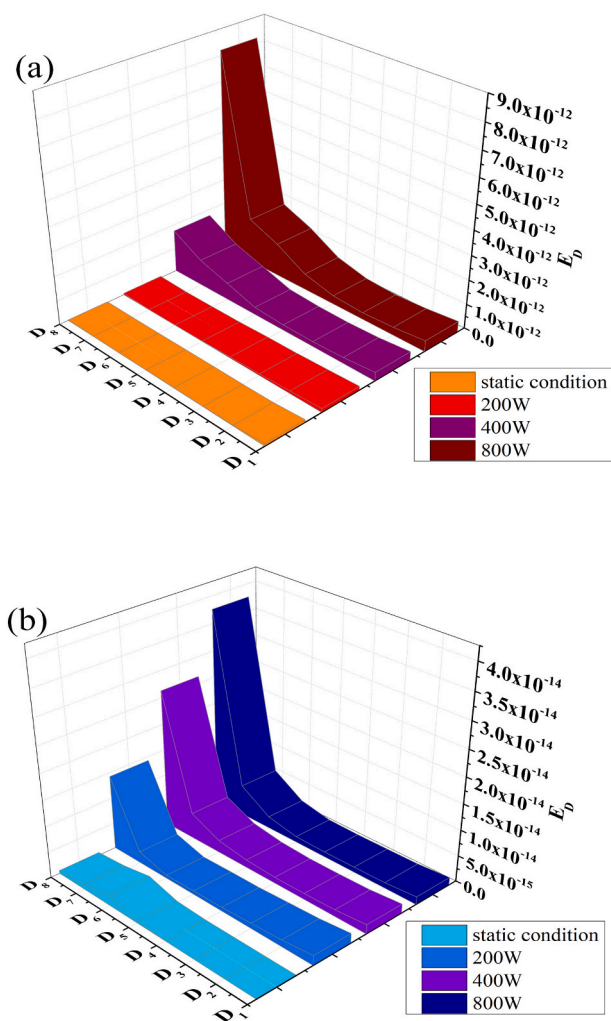
by the presence of aggressive Cl$^-$ ions and oxygen bubbles of cavitation. However, in comparison, the cavitated surface of the NbC coating remains intact with a smooth appearance and with no evidence of plastic deformation even at an output power of 800 W. As described in Section 3.2, because the NbC coating has a much higher hardness and H/E ratio than uncoated Ti-6Al-4V, the NbC coating deforms in a predominantly elastic manner under cavitation erosion condition and the coating can efficiently absorb the energy of the collapsing bubbles, due to its higher elastoplasticity. At output power values of 400 and 800 W, numerous very shallow and small grooves were visible on the cavitated surface of the coating due to the preferential attack of local region, resulting in a granular morphology. Overall, the surface morphology evolution for the NbC coating with output power is consistent with the electrochemical results.

4. Conclusions

NbC nanocrystalline coating was prepared onto Ti-6Al-4V alloy substrate to improve its cavitation erosion-corrosion resistance in 3.5 wt % NaCl solution. Following characterization of microstructure and mechanical properties of the coating, the corrosion resistance of the coating under cavitation erosion condition was investigated. The following conclusions can be drawn:

(1) The coating consists of equiaxed δ-NbC crystals with an average grain size of ~10 nm and a strong (200) preferred orientation. The H/E ratio, used as an index of predicting the cavitation erosion resistance, is much higher for the coating (0.085) than that for the alloy substrate (0.043).

(2) The analysis of EN in the time domain suggests that the calculated Rn value of the coating is almost insensitive to the output powers and is one order of magnitudes larger than that of the Ti-6Al-4V substrate at the output power of 800 W. Shot noise analysis shows that after coated with the NbC coating, the distribution of f_n shifts to a higher frequency region and, simultaneously, the upper limit of the q values is dropped by four-fold under cavitation condition, indicative of an excellent protection afforded by the NbC coating.

(3) The frequency domain analysis shows that for uncoated Ti-6Al-4V, the k values for current and potential PSD are higher than-20 dB/decade at the output powers at 400 and 800 W, whereas the k values for the coating are always lower than −20 dB/decade even at an output power of 800 W, indicating that the coating exhibits a higher resistance to pitting corrosion.

(4) The discrete wavelet-transform results of the electrochemical noise suggest that compared with bare Ti-6Al-4V, the total energy accumulated by in the d series crystals for the coating is reduced by 2 orders of magnitude, suggesting a decrease in the electrochemical activity.

CRediT authorship contribution statement

Shuang Peng: Conceptualization, Investigation. **Jiang Xu:** Writing – original draft. **Zhengyang Li:** Resources. **Shuyun Jiang:** Formal analysis. **Zong-Han Xie:** Data curation. **Paul Munroe:** Writing – review & editing.

Declaration of competing interest

The authors declare that they have no known competing financial interests or personal relationships that could have appeared to influence the work reported in this paper.
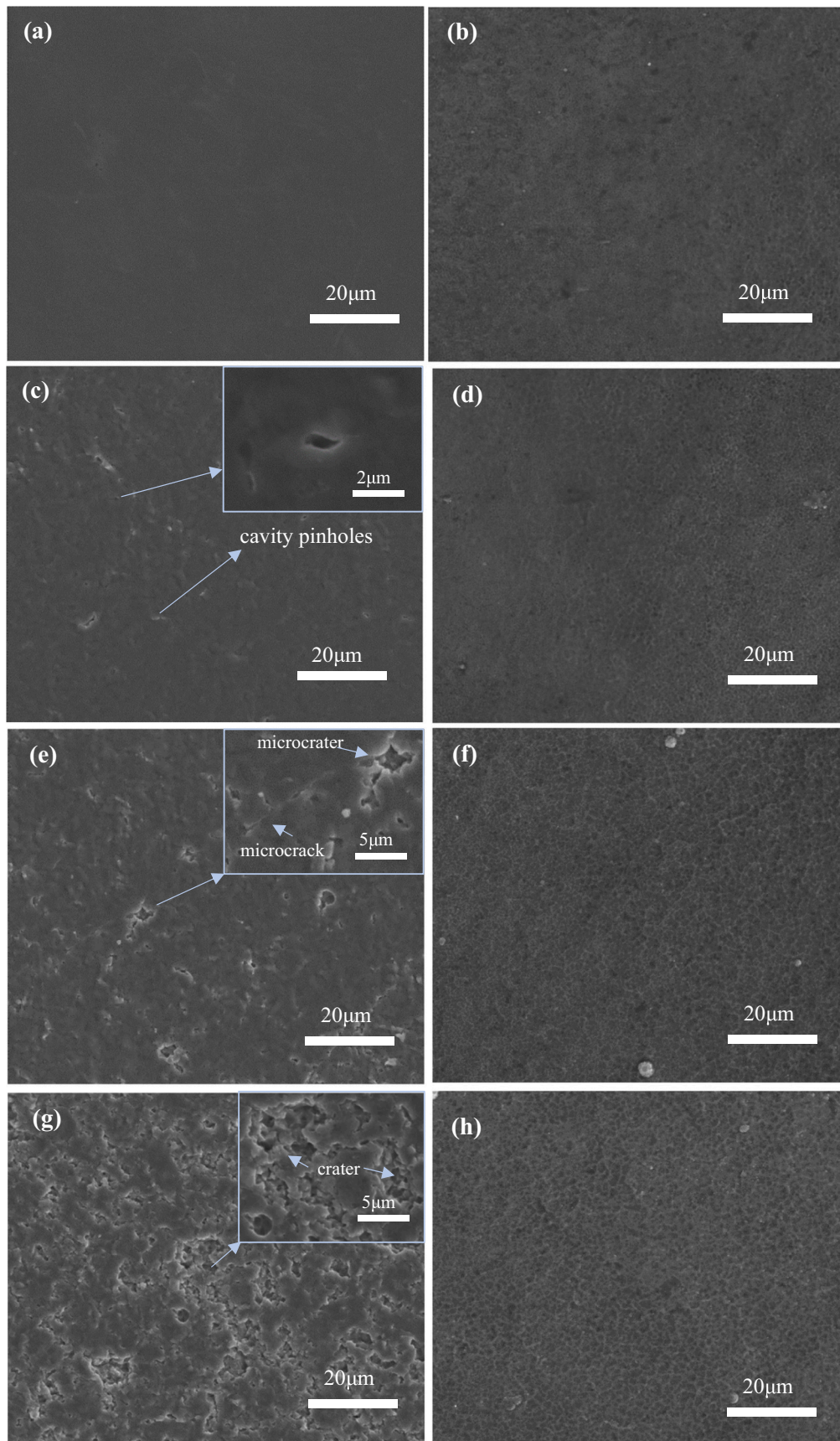
Fig. 14. The energy distribution plots (EDPs) corresponding to the current noise signals for (a) the uncoated Ti-6Al-4V and (b) NbC coating after an exposure time of 6 h in a 3.5 wt% NaCl solution under static conditions and cavitation erosion conditions at output power levels of 200 W, 400 W and 800 W, respectively.

surface. When the output power increases to 400 W, the cavitated surface becomes rougher with many surface undulations and numerous microcraters and microcracks. The repeated mechanical impact induced by high velocity micro-jets and shock waves not only promotes local plastic deformation, but also lead to work-hardening of the surface layer and eventually the formation of the microcracks or microcraters [57]. Along with these cracks' propagation, they begin to connect with each other and small number of materials is subsequently peeled off the surface to generate large microcraters. The noticeable changes in cavitated surface morphologies corresponding to the increase of the output power from 200 W to 400 W are consistent with the marked changes in the patterns of current noises and analysis of the relevant parameters. A further increase in the output power, the microcraters and micropits spread almost the entire cavitated surface, making it much rougher and looser, suggesting that Ti-6Al-4V alloy suffers severer cavitation damage. Such a severe cavitation degradation of uncoated Ti-6Al-4V is closely tied to the synergism between the mechanical factors arising from the cavitation impacts and the electrochemical factors generated

Fig. 15. Secondary electron images of the eroded surface morphologies of (a, c, e and g) the Ti-6Al-4V substrate and (b, d, f and h) the NbC coating after a 6 h exposure in a 3.5 wt% NaCl solution under (a and e) static electrolyte and cavitation erosion conditions with output power levels of (c and d) 200 W, (e and f) 400 W and (g and h) 800 W..

Acknowledgements

Data availability

The raw/processed data required to reproduce these findings cannot be shared at this time as the data also forms part of an ongoing study.

References

[1] J. Lin, Z. Wang, J. Cheng, M. Kang, X. Fu, S. Hong, Evaluation of cavitation erosion resistance of arc-sprayed Fe-based amorphous/nanocrystalline coatings in NaCl solution, Results Phys. 12 (2019) 597–602.

[2] J. Basumatary, R.J.K. Wood, Different methods of measuring synergy between cavitation erosion and corrosion for nickel aluminium bronze in 3.5% NaCl solution, Tribol, Int. 147 (2020), 104843.

[3] C.T. Kwok, F.T. Cheng, H.C. Man, Synergistic effect of cavitation erosion and corrosion of various engineering alloys in 3.5% NaCl solution, Mater. Sci. Eng. A 290 (2000) 145–154.

[4] M. Abedini, F. Reuter, S. Hanke, Corrosion and material alterations of a CuZn38Pb3 brass under acoustic cavitation, Ultrason, Sonochem. 58 (2019), 104628.

[5] Z. Dong, T. Zhou, J. Liu, X. Zhang, B. Shen, W. Hu, L. Liu, Cavitation erosion behaviors of surface chromizing layer on 316L stainless steel, Ultrason, Sonochem. 58 (2019), 104668.

[6] A. Neville, B.A.B. McDougall, Erosion- and cavitation-corrosion of titanium and its alloys, Wear 250 (2001) 726–735.

[7] R. Singh, S.K. Tiwari, S.K. Mishra, Cavitation erosion in hydraulic turbine components and mitigation by coatings: current status and future needs, J. Mater. Eng. Perform. 21 (2012) 1539–1551.

[8] J. Xu, W. Hu, Z.H. Xie, P. Munroe, Reactive-sputter-deposited β-Ta$_2$O$_5$ and TaON nanoceramic coatings on Ti-6Al-4V alloy against wear and corrosion damage, Surf, Coat. Tech. 296 (2016) 171–184.

[9] J. Xu, L. Liu, Z.H. Xie, P. Munroe, Nanocomposite bilayer film for resisting wear and corrosion damage of a Ti-6Al-4V alloy, surf, Coat. Tech. 206 (2012) 4156–4165.

[10] J. Xu, S.K. Zhang, X.L. Lu, S. Jiang, P. Munroe, Z.H. Xie, Effect of Al alloying on cavitation erosion behavior of TaSi$_2$ nanocrystalline coatings, Ultrason, Sonochem. 59 (2019), 104742.

[11] J. Xu, S. Peng, Z. Li, S. Jiang, Z.H. Xie, P. Munroe, The influence of semiconducting properties of passive films on the cavitation erosion resistance of a NbN nanoceramic coating, Ultrason, Sonochem. 71 (2021), 105406.

[12] S. Hong, Y. Wu, J. Zhang, Y. Zheng, Y. Zheng, J. Lin, Synergistic effect of ultrasonic cavitation erosion and corrosion of WC–CoCr and FeCrSiBMn coatings prepared by HVOF spraying, Ultrason, Sonochem. 31 (2016) 563–569.

[13] K. Zhang, M. Wen, G. Cheng, X. Li, Q.N. Meng, J.S. Lian, W.T. Zheng, Reactive magnetron sputtering deposition and characterization of niobium carbide films, Vacuum 99 (2014) 233–241.

[14] F.A.P. Fernandes, J. Gallego, C.A. Picon, G. Tremiliosi Filho, L.C. Casteletti, Wear and corrosion of niobium carbide coated AISI 52100 bearing steel, Surf, Coat. Technol. 279 (2015) 112–117.

[15] I.C. Park, S.J. Kim, Cavitation erosion behavior in seawater of electroless Ni-P coating and process optimization using Taguchi method, Appl, Surf. Sci. 477 (2019) 37–43.

[16] J. Liu, Y. Lin, X. Yong, X. Li, Study of cavitation corrosion behaviors and mechanism of carbon steel in neutral sodium chloride aqueous solution, Corrosion 61 (2005) 1061–1069.

[17] I. Mitelea, E. Dimian, I. Bordeasu, C. Crăciunescu, Ultrasonic cavitation erosion of gas nitrided Ti-6Al-4V alloys, Ultrason, Sonochem. 21 (2014) 1544–1548.

[18] J. Ryl, J. Wysocka, P. Slepski, K. Darowicki, Instantaneous impedance monitoring of synergistic effect between cavitation erosion and corrosion processes, Electrochim. Acta 203 (2016) 388–395.

[19] S. Hong, Y. Wu, J. Zhang, Y. Zheng, Y. Qin, J. Lin, Effect of ultrasonic cavitation erosion on corrosion behavior of high-velocity oxygen-fuel (HVOF) sprayed near-nanostructured WC-10Co-4Cr coating, Ultrason, Sonochem. 27 (2015) 374–378.

[20] R.A. Cottis, Interpretation of electrochemical noise data, Corrosion 57 (2001) 265–285.

[21] J.B. Shi, J.H. Wang, K. Wang, D.H. Xia, Electrochemical noise study on the corrosion behavior of 304NG stainless steel in high temperature water, Electrochemistry 82 (2014) 647–653.

[22] R.J.K. Wood, J.A. Wharton, A.J. Speyer, K.S. Tan, Investigation of erosion–corrosion processes using electrochemical noise measurements, Tribol, Int. 35 (2002) 631–641.

[23] W.C. Oliver, G.M. Pharr, An improved technique for determining hardness and elastic modulus using load and displacement sensing indentation experiments, J. Mater. Res. 7 (1992) 1564–1583.

[24] D.S. Rickerby, A.M. Jones, B.A. Bellamy, X-ray diffraction studies of physically vapour-deposited coatings, Surf, Coat. Technol. 37 (1989) 111–137.

[25] V. Chawla, R. Jayaganthan, R. Chandra, Structural characterizations of magnetron sputtered nanocrystalline TiN thin films, Mater. Charact. 59 (2008) 1015–1020.

[26] M.I. Jones, I.R. McColl, D.M. Grant, Effect of substrate preparation and deposition conditions on the preferred orientation of TiN coatings deposited by RF reactive sputtering, Surf, Coat. Technol. 132 (2000) 143–151.

[27] R.A. Mesquita, C.A. Schuh, Tool steel coatings based on niobium carbide and carbonitride compounds, Surf, Coat. Technol. 207 (2012) 472–479.

[28] A.L. Patterson, The Scherrer formula for X-ray particle size determination, Phys. Rev. 56 (1939) 978–982.

[29] M. E, H.X. Hu, X.M. Guo, Y.G. Zheng, Comparison of the cavitation erosion and slurry erosion behavior of cobalt-based and nickel-based coatings, Wear 428-429 (2019) 246–257.

[30] C.H. Tang, F.T. Cheng, H.C. Man, Laser surface alloying of a marine propeller bronze using aluminium powder: part I: microstructural analysis and cavitation erosion study, Surf, Coat. Technol. 200 (2006) 2602–2609.

[31] A. Krella, The influence of TiN coatings properties on cavitation erosion resistance, Surf. Coat. Technol. 204 (2009) 263–270.

[32] H.R. Bakhshandeh, S.R. Allahkaram, A.H. Zabihi, An investigation on cavitation-corrosion behavior of Ni/β-SiC nanocomposite coatings under ultrasonic field, Ultrason, Sonochem. 56 (2019) 229–239.

[33] S.Z. Luo, Y.G. Zheng, M.C. Li, Z.M. Yao, W. Ke, Effect of cavitation on corrosion behavior of 20SiMn low-alloy steel in 3% sodium chloride solution, Corrosion 59 (2003) 597–605.

[34] B.C. Wang, J.H. Zhu, Influence of ultrasonic cavitation on passive film of stainless steel, Ultrason, Sonochem. 15 (2008) 239–243.

[35] X. Yong, D. Li, H. Shen, Electrochemical responses to degradation of the surface layer nano-mechanical properties of stainless steels under cavitation, Mater. Chem. Phys. 139 (2013) 290–297.

[36] A. Darlinski, J. Halbritter, Angle-resolved XPS studies of oxides at NbN, NbC, and Nb surfaces, Surf, Interface Anal. 10 (1987) 223–237.

[37] A. OrjuelaG, R. Rincon, J.J. Olaya, Corrosion resistance of niobium carbide coatings produced on AISI 1045 steel via thermo-reactive diffusion deposition, Surf, Coat. Technol. 259 (2014) 667–675.

[38] L. Wang, J. Sun, B. Kang, S. Li, S. Ji, Z. Wen, X. Wang, Electrochemical behaviour and surface conductivity of niobium carbide-modified austenitic stainless steel bipolar plate, J. Power Sources 246 (2014) 775–782.

[39] N. Nedfors, O. Tengstrand, A. Flink, A.M. Andersson, P. Eklund, L. Hultman, U. Jansson, Reactive sputtering of NbC$_x$-based nanocomposite coatings: An up-scaling study, Surf, Coat. Tech. 253 (2014) 100–108.

[40] L. von Fieandt, K. Johansson, E. Lindahl, T. Larsson, M. Boman, D. Rehnlund, Corrosion properties of CVD grown Ti(C,N) coatings in 3.5 wt-% NaCl environment, Corros, Eng. Sci. Techn. 53 (2018) 316–320.

[41] F.E. Castillejo, D.M. Marulanda, J.J. Olaya, J.E. Alfonso, Wear and corrosion resistance of niobium-chromium carbide coatings on AISI D2 produced through TRD, Surf, Coat. Tech. 254 (2014) 104–111.

[42] S. Ningshen, U. Kamachi Mudali, V.K. Mittal, H.S. Khatak, Semiconducting and passive film properties of nitrogen-containing type 316LN stainless steels, Corros, Sci. 49 (2007) 481–496.

[43] I.B. Obot, I.B. Onyeachu, A. Zeino, S.A. Umoren, Electrochemical noise (EN) technique: review of recent practical applications to corrosion electrochemistry research, J. Adhes. Sci. Technol. 33 (2019) 1453–1496.

[44] F. Mansfeld, Z. Sun, C.H. Hsu, A. Nagiub, Concerning trend removal in electrochemical noise measurements, Corros, Sci. 43 (2001) 341–352.

[45] D. Xia, S. Song, W. Gong, Y. Jiang, Z. Gao, J. Wang, Detection of corrosion-induced metal release from tinplate cans using a novel electrochemical sensor and inductively coupled plasma mass spectrometer, J. Food Eng. 113 (2012) 11–18.

[46] A. Legat, V. Doleček, Corrosion monitoring system based on measurement and analysis of electrochemical noise, Corrosion 51 (1995) 295–300.

[47] Y.F. Cheng, J.L. Luo, M. Wilmott, Spectral analysis of electrochemical noise with different transient shapes, Electrochim. Acta 45 (2000) 1763–1771.

[48] Y. Tan, Sensing localised corrosion by means of electrochemical noise detection and analysis, Sensor, Actuat. B 139 (2009) 688–698.

[49] J.M. Sanchez-Amaya, R.A. Cottis, F.J. Botana, Shot noise and statistical parameters for the estimation of corrosion mechanisms, Corros, Sci. 47 (2005) 3280–3299.

[50] J.M. Sánchez-Amaya, M. Bethencourt, L. González-Rovira, F.J. Botana, Noise resistance and shot noise parameters on the study of IGC of aluminium alloys with different heat treatments, Electrochim. Acta 52 (2007) 6569–6583.

[51] R.A. Cottis, Sources of electrochemical noise in corroding systems, Russ, J. Electrochem. 42 (2006) 497–505.

[52] A. Aballe, M. Bethencourt, F.J. Botana, M. Marcos, Using wavelets transform in the analysis of electrochemical noise data, Electrochim. Acta 44 (1999) 4805–4816.

[53] A. Aballe, M. Bethencourt, F.J. Botana, M. Marcos, Wavelet transform-based analysis for electrochemical noise, Electrochem. Commun. 1 (1999) 266–270.

[54] T. Zhang, Y. Shao, G. Meng, F. Wang, Electrochemical noise analysis of the corrosion of AZ91D magnesium alloy in alkaline chloride solution, Electrochim. Acta 53 (2007) 561–568.

[55] C. Yi, X. Du, Y. Yang, B. Zhu, Z. Zhang, Correlation between the corrosion rate and electrochemical noise energy of copper in chloride electrolyte, RSC Adv. 8 (2018) 19208–19212.

[56] J. Li, C.W. Du, Z.Y. Liu, X.G. Li, M. Liu, Effect of microstructure on the corrosion resistance of 2205 duplex stainless steel. Part 2: electrochemical noise analysis of corrosion behaviors of different microstructures based on wavelet transform, Constr, Build. Mater. 189 (2018) 1294–1302.

[57] G. Hou, Y. Ren, X. Zhang, F. Dong, X. An, X. Zhao, H. Zhou, J. Chen, Cavitation erosion mechanisms in Co-based coatings exposed to seawater, Ultrason, Sonochem. 60 (2020) 104799.